

Visualization Techniques for Molecular Dynamics

163



Jeffrey S. Kallman, Anthony J. De Groot, Carol G. Hoover, and William G. Hoover
Lawrence Livermore National Laboratory

Susanne M. Lee
Lawrence University

Frederick Wooten
University of California, Davis

To machine silicon surfaces economically using diamond turning machines requires understanding materials on the atomic level. One of the simplest experimental techniques for measuring a material's atomic ductile and brittle behavior is atomic-scale indentation, in which a small tool bit (approximately 100 atoms wide) is pressed into a micron-sized (10^{-6} meter) sample. We used nonequilibrium molecular dynamics to model this type of nano-indentation in pure silicon and studied the dependence of phase transformations on crystal temperature and indenter speed.¹

Electron and x-ray diffractometry visualize atoms in severely stressed single-crystal silicon and help analyze the resulting transformations. Massively parallel computers simulate both diffraction techniques.

We study these phase transitions with a number of simulation techniques. We calculate the position of the atoms in the material during the process and display atomic images of the crystal structure as a function of time. Simulated diffraction patterns enable us to follow structural transformations more easily. In addition, we have developed several diagnostic imaging techniques that aid the analysis of phase transformations: pair-correlation function, bar-code plotting, ring statistics, and subvolume visualization.

Molecular dynamics

Molecular dynamics simulations use atoms to model materials. The forces, interactions, and position of every atom are computed. Unfortunately, accurately predicting the behavior of materials in processes like the one we discuss here requires millions of atoms. Before the advent of parallel processing machines, which provide inexpensive speed and memory, such calculations were prohibitively expensive.

Molecular dynamics simulations require atomic force laws. We used the Stillinger-Weber potential for the atoms and modeled the tetrahedral-shaped indenter as either a smooth surface or an atomically rough one with the indenter atoms arranged in a diamond lattice.

Diagnostic techniques

As the indenter presses into the silicon workpiece, the crystal structure of the workpiece may change. Experimenters frequently study these changes using scanning tunneling microscopy, x-ray diffraction, and electron diffraction. Combining our calculated atomic positions with the silicon atomic radius, we form 3D images of the sample using either a z-buffer renderer² or a ray-tracing renderer.³ Miyamoto, Hattori, and Inui⁴ similarly visualized the atomic positions of atoms calculated by molecular dynamics.

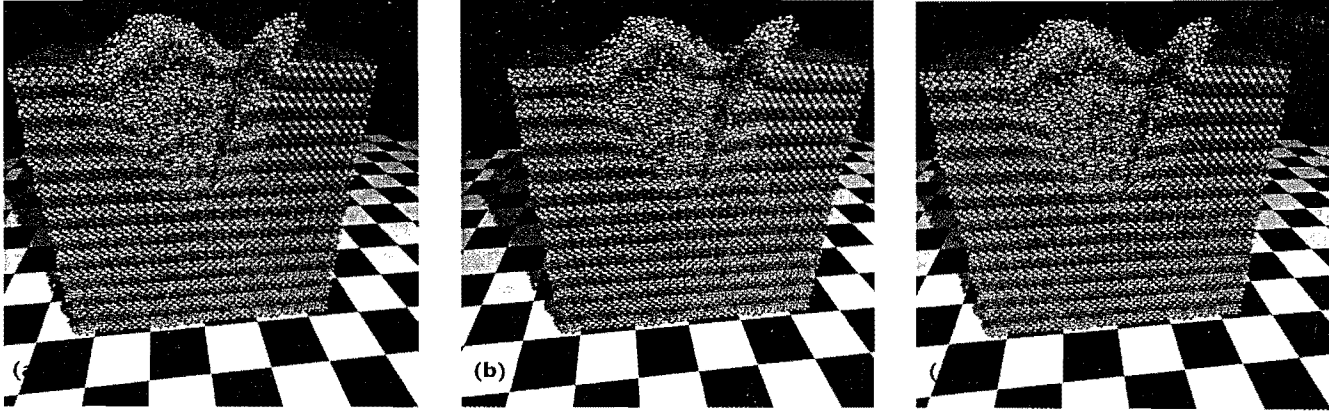
We found that assigning colors to the atoms based on their initial positions in the sample made the time evolution of the structure more apparent. Figure 1 shows that near the indenter, the regular array of atoms in the diamond structure changes, while several monolayers away, the silicon crystal structure remains unaffected by the process.

To analyze these different crystal structures in more detail, we simulated x-ray and electron diffraction.^{5,6} We simulate x-ray diffraction by defining a phase, $\Phi(\mathbf{r}, \mathbf{k}) = (2\pi\mathbf{r}\cdot\mathbf{k})/\lambda$, at each atomic scatterer position, \mathbf{r} , where \mathbf{k} is a unit vector consisting of the direction cosines of the x-ray beam, and λ is the wavelength of the x-ray beam, as shown in Figure 2.

We assume that every atom scatters isotropically by absorbing an x-ray of a particular phase and then re-emitting it as a spherical wave. In addition, we assume that the emitted wave is not disturbed on its way to the target. The target pixel array is defined as a circular one-dimensional ring of pixels. For every pixel in the target array, we determine the distance from each scatterer to the pixel, d , and add the real and imaginary parts of the scatterer wavefunction originating at \mathbf{r} .

Differences in distance from the scatterers to the pixels and in the initial scatterer wavefunction phases mean the wavefunctions from the individual scatterers have different phases and interfere at the pixel (see Figure 3). This interference causes intensity differences on the target ring of pixels when the magnitude of the sum of the complex numbers is written as the image.

Parallel computation ideally suits this problem. The



1 Cut-away view of crystalline silicon atoms indented with a tetrahedrally shaped diamond indenter. (a) and (b) form a cross fusion stereo image and should be viewed with crossed eyes. (b) and (c) form the same stereo pair, but should be viewed wall-eyed.

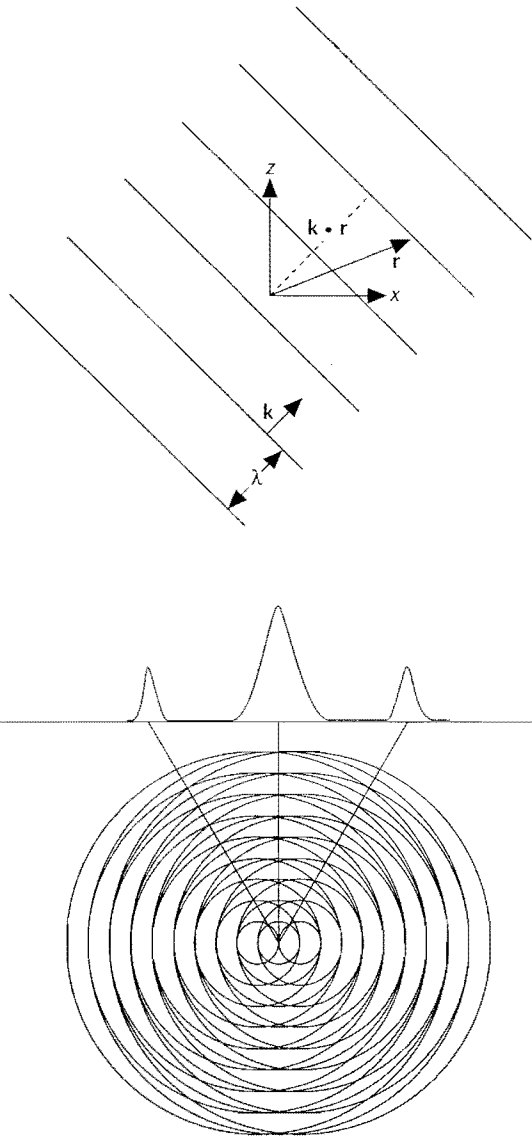
array of target pixels is distributed among the processors, and the scatterers' positions are broadcast to the processors. Figures 4 and 5 display these diffraction results for two different crystal structures: single-crystal and amorphous silicon.

Electron wavelengths are almost two orders of magnitude smaller than x-ray wavelengths, and the electrons frequently undergo multiple atomic scatterings. While simulated x-ray diffraction resembles holography,⁷ simulated electron diffraction resembles radiosity.⁸

In our electron diffraction simulation, we uniformly illuminate the silicon workpiece with electrons. (Fan described another way of simulating electron diffraction.⁹) We make the following assumptions to simplify the simulation of the electron scattering:

1. Electrons are emitted isotropically from point atoms.
2. The probability of an electron emitted from one atom being absorbed by another atom is proportional to the fraction of absorber atom cross section visible from the emitter atom.
3. The source electron flux is uniform throughout the entire sample and has a phase similar to that in the x-ray simulation.

The electrons travel from atom to atom, and their phases and amplitudes are modified with each atomic interaction. The atom-to-atom form factors are complex rather than real. The magnitude of the atom-to-atom form factors represents the fraction of electrons leaving one atom and landing on

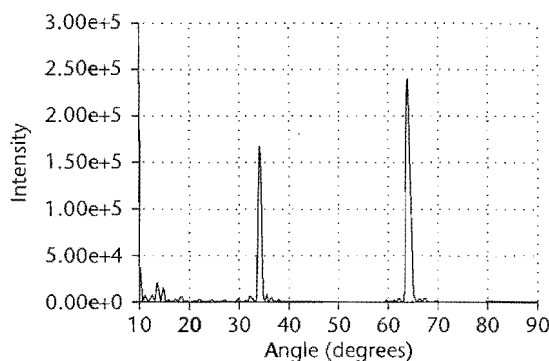


2 Schematic showing the relation of the incident x-ray plane wave to the phase of the spherical x-ray wave emitted by an atom. The origin is an arbitrary point where the phase is defined as zero, the position vector r points from the origin to an atom in the sample, the k vector is the direction cosine vector of the x-ray plane wave, and λ is the x-ray wavelength. Each atom absorbs plane-wave x-rays of a phase, then emits spherical x-ray waves with that phase.

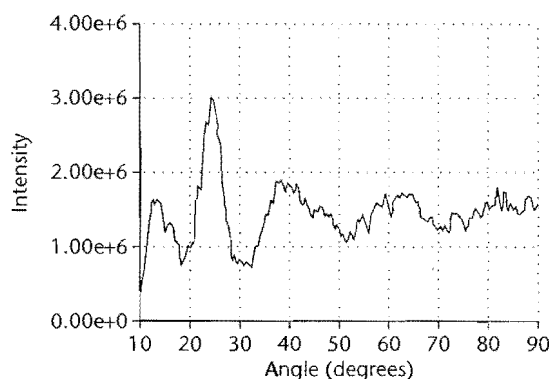
3 The moiré pattern shown here illustrates how the maxima and minima in the interference pattern arise. The straight lines show the directions along which maxima occur.

another atom, while the phase of the form factors represents the change in phase of those electron wavefunctions. We calculate these complex form factors using a

4 Simulated angle-resolved x-ray diffraction image of unindented diamond cubic crystalline silicon oriented along the (100) plane. The x-ray wavelength was $1.5405\text{\AA} = 1.5405 \times 10^{-10}$ meters.



5 Simulated angle-resolved x-ray diffraction image of unindented amorphous silicon. The x-ray wavelength was 1.5405\AA .



modification of the hemicube method.¹⁰ The modification uses a cube of z-buffers instead of the standard half cube because we assume the atoms are point emitters.

Then we follow the typical radiosity procedure, computing the form factors from atom i to atom j , F_{ij} . A matrix equation containing the initial phases and amplitudes, I_j , of the electron wavefunctions is solved. The

view of the atoms in Figure 1 plus the x-ray and electron diffraction simulations, it is difficult to determine where the workpiece has truly been amorphized and where it is still crystalline but with some disorder. There are two solutions to this problem: (1) plot a pair-correlation function versus distance between atoms in the workpiece or (2) perform an atomic ring-count diagnostic.

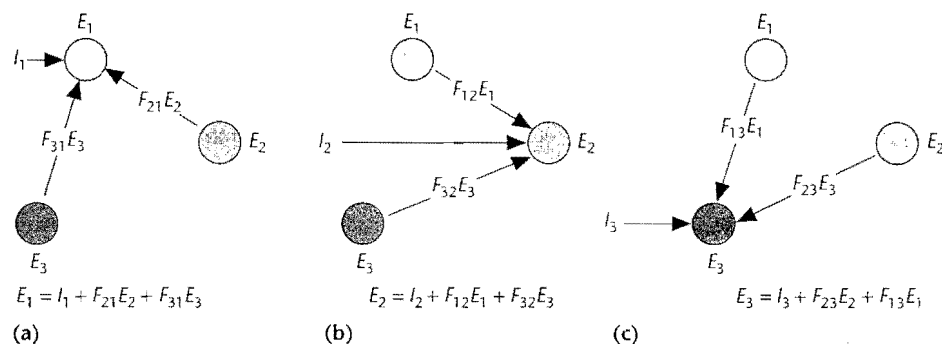
solution consists of the modified phases and amplitudes, E_j , of the electron wavefunctions. Figure 6 illustrates the derivation of this matrix equation.

$$\begin{pmatrix} 1 & -F_{21} & -F_{31} \\ -F_{12} & 1 & -F_{32} \\ -F_{13} & -F_{23} & 1 \end{pmatrix} \begin{pmatrix} E_1 \\ E_2 \\ E_3 \end{pmatrix} = \begin{pmatrix} I_1 \\ I_2 \\ I_3 \end{pmatrix}$$

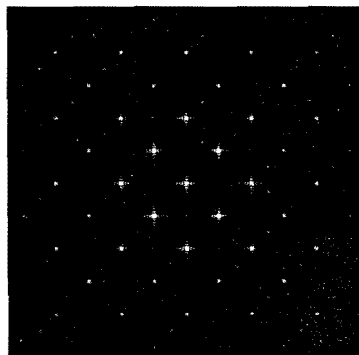
Thereafter, we produce images using the computed phases and amplitudes in the same way as in x-ray imaging, except that the target pixel array is now a 2D array instead of a 1D ring. Figures 7 and 8 show simulated electron diffraction of crystalline and amorphous silicon.

Our indentation simulations showed us that the workpiece becomes only partially disordered during the indentation process. As Figure 1 shows, a gradual transition takes place from the heavily disordered material near the indenter to the single-crystal material far from the indenter. Taking just the direct

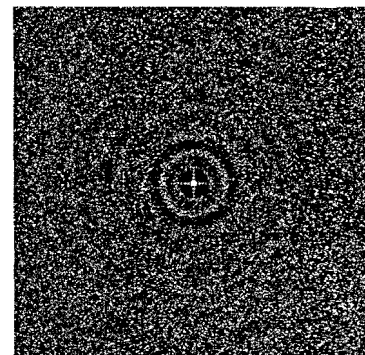
6 Derivation of the matrix equation for electron diffraction. (a), (b), and (c) show, respectively, the derivations of rows one, two, and three of the matrix.

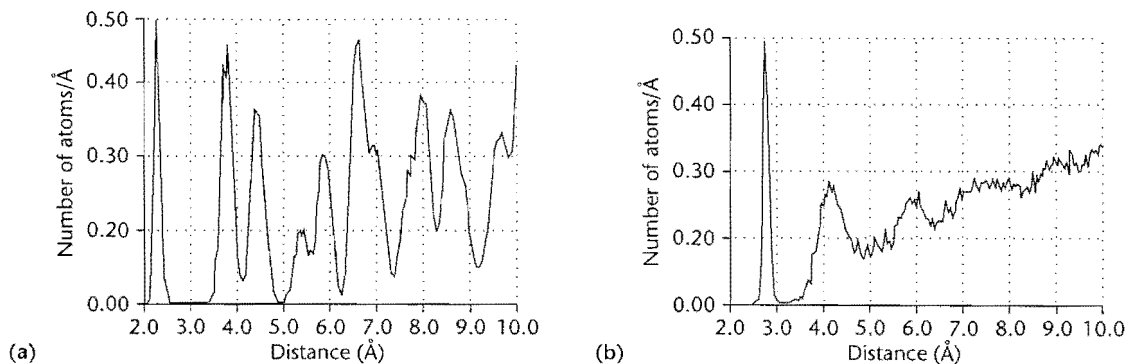


7 Simulated electron diffraction image of unindented diamond cubic crystalline silicon oriented along the (100) plane. The electron wavelength was $0.03747\text{\AA} = 3.747 \times 10^{-12}$ meters.



8 Simulated electron diffraction image of unindented amorphous silicon. The electron wavelength was 0.03747\AA .





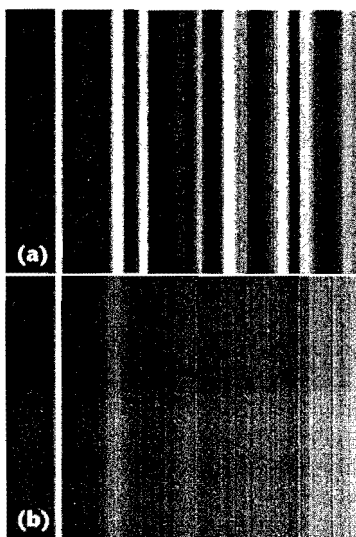
9 Graph of the pair correlation function showing the number of atoms a given distance away from each atom in the sample normalized by the distance between the atoms. (a) Pair correlation for unindented diamond cubic crystalline silicon. (b) Pair correlation for unindented amorphous silicon demonstrating the absence of the third (crystalline) peak at approximately 4.5Å.

The pair-correlation function for a heavily disordered crystal differs from that for an amorphous sample. Figure 9 shows a pair-correlation plot for a crystalline sample and for an amorphous sample. The significant distinguishing feature is the absence of the third (crystal) peak in the amorphous sample.

A simpler way of visualizing this pair-correlation function is to assign a grayscale value to each intensity in the pair-correlation function and then display the intensities as a function of distance. The resulting pictures resemble bar codes, so we named them bar-code plots. Figure 10 shows the bar-code plots corresponding to the curves in Figure 9.

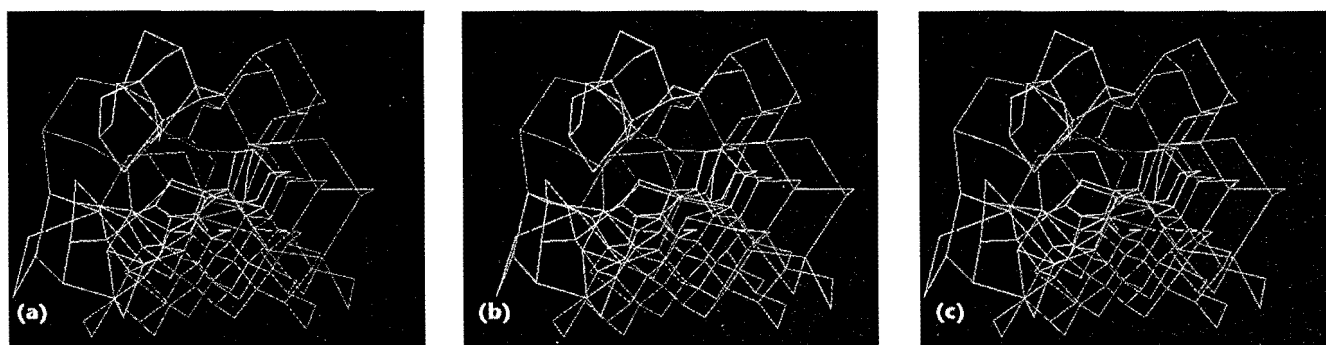
In the atomic ring-count diagnostic, we count the number of steps required to complete a closed loop by moving from atom to atom along a covalently bonded chain. In the diamond cubic crystal structure, it is possible to do this in six, eight, or any higher even number of moves. There are no rings that allow return in an odd number of moves. In amorphous silicon, however, nearly every atom is a member of five- or seven-atom rings. Looking at the proportion of five- and seven-member rings to six- and eight-member rings indicates the proportion of a sample that is amorphous.

In our indentation simulations, we find rings of odd



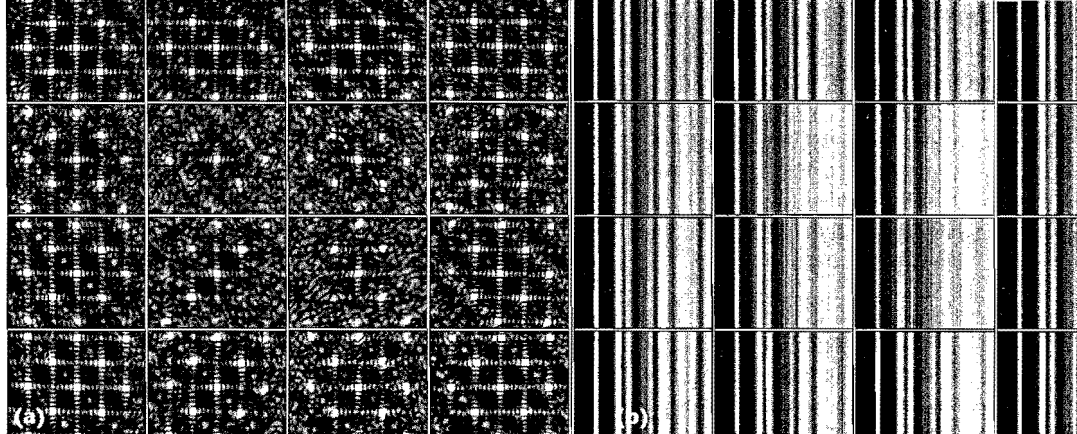
10 Bar-code plots of the pair correlation functions shown in Figure 9 for (a) unindented diamond cubic crystalline silicon and (b) unindented amorphous silicon.

and even length around the site of indentation, from which we deduce that our sample was amorphized during the indentation process. Figure 11 displays a stereo pair of images showing the rings extracted from our indentation simulation.



11 Stereo image of rings found in a section of the sample near the indenter tip. The green loops correspond to six-membered rings, the red loops correspond to all other even-membered rings, and the yellow loops correspond to all odd-membered rings. The yellow loops were drawn last and might, therefore, overlap a few even-membered ring links. (a) and (b) should be viewed with crossed eyes and (b) and (c) should be viewed wall-eyed.

12 Subvolume visualization by (a) x-ray diffraction ($\lambda = 0.03747\text{\AA}$) and (b) barcode plots of the sample material near the indenter tip.



13 X-ray diffraction of the same sample volume as shown in Figure 12. This diffraction image implies the complete sample is crystalline, yet the subvolume images in Figure 12 clearly demonstrate this is not the case.



To determine the locations of the critical deforming regions, we divide the sample into small pieces and then apply the diagnostics described above to each piece individually. Examples of x-ray diffraction patterns and bar codes appear in Figure 12, revealing the transition region from amorphous to crystalline volumes of sample. The subvolumes in Figure 12 contain the region that surrounds the indenter tip. The center four squares show the diffuse rings indicative of amorphous material, while the surrounding material remains single crystal. The indistinctness of the diffraction patterns in the subvolumes results from a fundamental limitation of this technique: As the number of atoms in each small region decreases, the signal-to-noise level falls significantly.

Figure 13 shows an x-ray diffraction pattern from all the atoms used to produce the 16 diffraction patterns of Figure 12. From the sharpness of the spots in Figure 13, the diffracted material appears crystalline, yet from Figure 12 we know it is a mixture of amorphous and crystalline material.

Conclusion

These techniques grew out of our attempts to provide experimentalists with a familiar way of looking at simulation data. Diffraction images are typically the raw data from which researchers draw experimental conclusions, and we found images based on simulations of diffraction techniques to be as meaningful as the other

diagnostics we used (pair correlation functions, ripples, and atomic imaging). The slicing of the position data into subvolumes made the diffraction techniques more useful than they would be in an experimental setting.

In the future it should be possible to build a software system that applies all of these diagnostics at once. An analyst would select a relative volume of action for a diagnostic (centered on the current position), then slice through the simulation data.

Acknowledgments

We would like to thank Charles W. Grant for a review of this manuscript. This work was performed under the auspices of the United States Department of Energy by Lawrence Livermore National Laboratory under contract number W-7405-ENG-48.

References

1. J.S. Kallman et al., "Molecular Dynamics of Elastic Flow: Indentation of Stillinger-Weber Silicon," *Phys. Rev. B*, Vol. 47, 1993, pp. 7705-7709.
2. E. Catmull, *A Subdivision Algorithm for Computer Display of Curved Surfaces*, doctoral dissertation, Tech. Report CSC-74-133, University of Utah, Provo, Dec. 1974.
3. T.J. Whitted, "An Improved Model for Shaded Displays," *Comm. ACM*, Vol. 23, No. 6, June 1980, pp. 343-344.
4. A. Miyamoto, T. Hattori, and T. Inui, "Structural Dynamics of Oxide Superconductor Films as Investigated by Molecular Dynamics and Computer Graphics," *J. Comput. Phys.*, Vol. 190, Nos. 1 and 2, Dec. 1991, pp. 93-96.
5. K. Rajendran, "Simulation of Diffraction Patterns of Crystalline and Amorphous Bodies," *Materials Characterization and Physics*, Vol. 28, 1991, pp. 337-344.
6. J.K. Steele and R.R. Biederman, "Computer-Aided Simulation and Analysis of Electron and X-Ray Diffraction Patterns," *Materials Characterization*, Vol. 27, No. 4, Dec. 1991, pp. 213-221.
7. A.D. Stein, Z. Wang, and J.S. Leigh, Jr., "Computer-Generated Holograms: A Simplified Ray-Tracing Approach," *Computers in Physics*, Vol. 6, No. 4, July/Aug. 1992, pp. 389-392.
8. C.M. Goral, K.E. Torrance, D.P. Greenberg, and B.B.

"Modeling of the Interaction of Light between Diffuse Surfaces," *Computer Graphics* (Proc. Siggraph 84), Vol. 18, No. 3, July 1984, pp. 213-221.

9. G.Y. Fan, "Electron Diffraction Simulation on Micro-VAX II Computers with the Aid of an Array Processor," *Computer Physics Comm.*, Vol. 59, No. 2, June 1990, pp. 429-438.
10. M.F. Cohen and D.P. Greenberg, "The Hemi-Cube: A Radiosity Solution for Complex Environments," *Computer Graphics* (Proc. Siggraph 85), Vol. 19, No. 3, July 1985, pp. 31-40.



Carol G. Hoover is a computational plasma physicist at Lawrence Livermore National Laboratory. Her most recent work involves developing parallel algorithms for the explicit continuum model, Dyna3D. She received a BS in physics from Auburn University, Alabama, in 1967 and a PhD in engineering and applied science from the University of California at Davis/Livermore in 1978.



Jeffrey S. Kallman works for Lawrence Livermore National Laboratory. His research focuses on underground imaging inverse problems, computed holography, and electrodynamic simulation programs in the service of integrated optics. He received a BS in engineering from Harvey Mudd College, Claremont, Calif., in 1979, an MS in electrical and biomedical engineering from Carnegie Mellon University, Pittsburgh, in 1981, and a PhD in engineering applied science from the University of California, Davis, in 1994.



William G. Hoover worked as a physicist at Lawrence Livermore National Laboratory and as a professor of engineering in the Department of Applied Science at the University of California at Davis/Livermore. He retired in 1994 to complete his third book, *Computer Simulation of Classical Thermomechanical Systems* (in preparation for Springer-Verlag). He received a BA in chemical physics from Oberlin College in 1958 and MS and PhD degrees from the University of Michigan (1961), followed by a postdoctoral fellowship at Duke University from 1961 to 1962. He is a fellow of the American Physical Society.



Susanne M. Lee is an assistant professor of physics at Lawrence University in Wisconsin, where her research has focused on solid-state phase transformations in binary semiconductors. She was at the Lawrence Livermore National Laboratory on a Post College Appointment Fellowship as a postdoctoral fellow from 1991 to 1993. She received a BS in engineering and applied physics in 1983 and a PhD in applied physics in 1990 from Harvard University.



Frederick Wooten is a professor of applied science at the University of California, Davis, where he served as department chairman from 1973 to 1992. His current interests are in the geometry and topology of amorphous materials and in computational group theory. He received a BS from Massachusetts Institute of Technology in 1950 and a PhD in chemistry from the University of Delaware in 1955. He is the author of *Optical Properties of Solids* (Academic Press, 1972).



Anthony J. De Groot is project leader of the Sprint Project at Lawrence Livermore National Laboratory and architect of the Sprint family of massively parallel multiprocessors. He is also a member of the Graduate Group of Computer Science at the University of California, Davis. He is currently designing a multiprocessor based on parallel fiber optic interconnects. He received a BS in electrical engineering in 1976, an MS in computer science in 1979, and a PhD in computer science in 1989, all from the University of California, Davis. He is a member of Tau Beta Pi, IEEE, and ACM.

Readers should contact Kallman at Lawrence Livermore National Laboratory, PO Box 808, Livermore, CA 94551-7808.